Sphinx Journal of Mathematical Sciences
1(1), 48–64, 2026
DOI: https://doi.org/10.64389/sjms.2026.011110
https://sphinxsp.org/journal/index.php/isp/

Research article

Thermoelastic-Diffusive Wave Reflection with Impedance, Hyperbolic Two-Temperature, and Temperature-Dependent Properties under the MGT Model

Saurav Sharma[1,*], Hazem Elsadek[2]

[1] 1277 Harrow Cres, Yardley, Pennsylvania-19067 USA, sauravkuk@gmail.com
[2] Department of computer science, Faculty of Computers and Information Systems, Egyptian Chinese University, Cairo, Egypt, hazem.elsadek@ecu.edu.eg
* **Correspondence:** sauravkuk@gmail.com

ARTICLE INFO

Keywords:
Thermoelastic diffusion; Moore–Gibson–Thompson model; impedance boundary; nonlocality; temperature-dependent properties; reflection coefficients

Mathematics Subject Classification:
74A15, 74A18

Important Dates:
Received: 2 December 2025
Revised: 29 December 2025
Accepted: 2 January 2026
Online: 3 January 2026

ABSTRACT

Plane-wave reflection from a homogeneous, isotropic thermoelastic-diffusion half-space is investigated within the Moore–Gibson–Thompson heat-conduction framework. The model incorporates hyperbolic two-temperature effects, temperature-dependent material properties, nonlocality, and mechanical, thermal, and diffusive impedance boundary conditions. Using potential-function decomposition and time-harmonic solutions, the governing equations are reduced to a dispersion relation describing coupled longitudinal (P), thermal (T), diffusive (P_0), and transverse shear (SV) modes. The corresponding reflection amplitude ratios are obtained from the boundary system for different incident waves. Numerical results demonstrate that the reflected amplitudes and their angular extrema are significantly affected by the thermal model, impedance parameters, temperature dependence, and nonlocal parameter. The formulation also recovers the temperature-independent, diffusion-free, elastic-diffusive, and zero-impedance limits. The results provide a basis for advanced material characterization and interpretation of geophysical wave responses.

1. Introduction

Classical thermoelasticity combines the equations of elasticity with Fourier heat conduction. Although this framework is effective for slowly varying thermal fields, Fourier's law implies instantaneous thermal propagation and is therefore inadequate for short-time, high-frequency, and microscale processes. Generalized thermoelastic theories were developed to restore finite thermal-wave speeds and introduce physically meaningful thermal relaxation. Lord and Shulman incorporated a single relaxation time into the heat-conduction equation [1], whereas Green and Lindsay introduced two relaxation times through the constitutive relations [2]. Green and Naghdi subsequently established thermodynamically consistent alternatives, including formulations that support undamped thermal waves and thermoelastic behavior without energy dissipation [3–5].

These developments, reviewed comprehensively by Chandrasekharaiah [6], provide the theoretical foundation for contemporary hyperbolic models of coupled thermomechanical transport. In many solids, however, thermal transport is accompanied by mass diffusion, and the resulting mechanical response cannot be described by thermoelasticity alone. Nowacki initiated the dynamical theory of diffusion in elastic media [7], and Sherief et al. later formulated a generalized thermoelastic-diffusion theory that couples displacement, temperature, and concentration fields [8]. Kumar and Kansal examined the associated dynamic problem in generalized thermoelastic diffusive media [9]. Subsequent studies demonstrated that thermo-diffusive coupling can substantially alter wave speeds, attenuation, mode conversion, and interfacial reflection. Representative extensions include wave interaction at fluid–bio-thermoelastic diffusive interfaces [10], reflection from thermo-diffusive half-spaces with voids [11], multiphase-lag thermoelastic diffusion with temperature-dependent properties [12], and diffusive microstretch thermoelasticity [13]. Collectively, these studies establish that diffusion is not a secondary correction but an active transport mechanism that can redistribute energy among mechanical, thermal, and concentration modes.

A second limitation of classical continuum models is their inability to capture size-dependent behavior when the structural length scale becomes comparable to the material's internal characteristic length. Nonlocal elasticity addresses this limitation by allowing the stress at a material point to depend on the strain field within a finite neighborhood. The conceptual basis was established by Eringen and Edelen [14], followed by Eringen's nonlocal thermoelastic formulation [15]. Yu et al. extended this idea by incorporating both nonlocal heat conduction and nonlocal elasticity [16], while Saeed and Abbas demonstrated that nonlocality can markedly modify thermoelastic responses at the nanoscale [17]. These findings are particularly relevant to microstructured solids, nanomaterials, thin films, and porous media, in which local constitutive laws may overpredict stiffness or fail to capture dispersive wave behavior. Despite this progress, the combined influence of nonlocality, thermoelastic diffusion, and higher-order heat transport on reflection under non-ideal boundary conditions remains incompletely understood.

Realistic thermal loading also requires recognition that elastic, thermal, and transport coefficients may vary with temperature. Ezzat et al. examined the temperature dependence of the elastic modulus in generalized thermoelasticity with thermal relaxation [18], and Wang et al. showed that temperature-dependent properties modify transient thermoelastic responses under thermal shock [19]. Related studies considered laser-pulse heating within a two-temperature framework [20], temperature-dependent nanobeam behavior [21], and micropolar thermoelasticity with voids, internal heat generation, and three-phase-lag conduction [22]. More recent analyses have extended these ideas to rotating thermoelastic-diffusion systems with multiphase delays [23] and nonlocal poro-thermoelastic media affected by gravity and temperature dependence [24]. These contributions demonstrate that constant-property assumptions can conceal substantial changes in wave speeds, attenuation, and coupling strength, particularly under rapid or intense thermal excitation.

Among modern finite-speed heat-conduction models, the Moore–Gibson–Thompson (MGT) equation has attracted particular interest because it regularizes thermal-wave propagation through a higher-order time derivative and supports a richer dispersive structure than first-order relaxation models. Quintanilla established an MGT-based thermoelastic theory [25], and subsequent work addressed MGT thermoelastic dielectrics [26] and the decay of radial solutions [27]. The model has also been applied to continuous heat-source problems [28] and dipolar thermoelastic bodies [29]. Recent studies have extended MGT thermoelasticity to solids with and without energy dissipation [30], micropolar thermoviscoelastic media with nonlocal and hyperbolic two-temperature effects [31], orthotropic photothermoelastic materials with temperature-dependent properties [32], and bio-thermoelastic wave reflection [33]. These studies confirm that MGT conduction can significantly modify attenuation, stability, and mode-conversion behavior, yet most existing analyses treat only a subset of the interacting mechanisms relevant to thermoelastic-diffusion interfaces.

The physical description becomes still richer when distinct conductive and thermodynamic temperatures, phase-lag effects, viscosity, and prestress are incorporated. Tzou's unified approach linked heat conduction across micro- and macroscales [34], while two-temperature wave reflection in micropolar media was examined by Sharma and Marin [35]. Elastodynamic interactions in nonlocal thermoelastic diffusion with phase lags were later investigated by Sharma et al. [36]. Related studies addressed thermomechanical interaction without energy dissipation [37]. The broader mathematical framework of dynamic coupled thermoelasticity was established earlier by Dhaliwal and Singh [38]. Together, these results indicate that small changes in constitutive coupling can produce large, mode-dependent variations in reflected amplitudes, especially at oblique incidence.

Despite substantial progress, a unified analysis combining thermoelastic diffusion, MGT heat conduction, nonlocality, temperature-dependent properties, initial stress, and impedance boundary conditions remains limited. The present study addresses this gap by formulating a plane-wave reflection model for a nonlocal thermoelastic-diffusion half-space governed by the MGT equation. The coupled longitudinal, thermal, diffusive, and shear modes are obtained from the dispersion relation, and their amplitude ratios are determined under mechanical, thermal, and diffusive impedance constraints. The numerical results clarify how nonlocality, temperature dependence, prestress, impedance, frequency, and incidence angle influence mode conversion and reflected-wave amplitudes, with potential applications in material characterization, interface design, and microstructured solids.

2. Governing Equations

The Following Abouelregal et al. [33] and Kumar et al. [10], the governing equations of the MGT thermoelastic-diffusion equations are considered without body forces, thermal and diffusion sources as:

$$t_{ij} = 2\mu e_{ij} + \delta_{ij}(\lambda_o e_{kk} - \gamma_1\theta - \gamma_2 P), \tag{2.1}$$

$$(\lambda_o + \mu)u_{j,ij} + \mu u_{i,jj} - \gamma_1\theta_{,i} - \gamma_2 P_{,i} = \rho\ (1 - \xi^2\nabla^2)\frac{\partial^2 u_i}{\partial t^2}, \tag{2.2}$$

$$\left(K\frac{\partial}{\partial t} + K^*\right)\varphi_{,ii} = \left(1 + \tau_o\frac{\partial}{\partial t}\right)\left(T_o l\ddot{\theta} + \gamma_1 T_o\ddot{e}_{kk} + dT_o\ddot{P}\right), \tag{2.3}$$

$$\left(D\frac{\partial}{\partial t} + D^*\right)P_{,ii} = \left(1 + \tau_1\frac{\partial}{\partial t}\right)\left(n\ddot{P} + \gamma_2\ddot{e}_{kk} + d\ddot{\theta}\right), \tag{2.4}$$

$$\ddot{\theta} = \ddot{\varphi} - \beta^*\nabla^2\varphi, \tag{2.5}$$

where

$$\lambda_o = \lambda - \frac{\beta_2^2}{b}, \quad \gamma_1 = \beta_1 + \beta_2 d, \quad \gamma_2 = \frac{\beta_2}{b}, \quad d = \frac{a}{b}, \quad n = \frac{1}{b}, \quad l = \frac{\rho C_e}{T_o} + \frac{a^2}{b}.$$

The temperature increment is defined by $\theta = T - T_o$, where T is the absolute temperature and T_o is the uniform reference temperature, subject to $\left\|\frac{T-T_o}{T_o}\right\| \ll 1$.

Here, ρ, C_e, P, t_{ij} and $u_i$denote density, specific heat, chemical potential, stress, and displacement, respectively. The parameters (τ_o , τ_1), (K,K^*)(D, D^*) represent thermal/diffusion lags, heat-conduction coefficients, and diffusion coefficients, while a and b characterize thermo-diffusive coupling. Moreover,

$\beta_1 = (3\lambda + 2\mu)\alpha_t$ and $\beta_2 = (3\lambda + 2\mu)\alpha_c$.

Where α_t, α_c are the thermal and diffusive expansion coefficients, and λ, μ are the Lamé constants. Commas denote spatial derivatives and overdots denote time derivatives. Temperature-dependent material properties are introduced through:

$$\lambda_0 = \lambda_{01}f(T), \ \ \mu = \mu_o f(T)\ , \ \ K = K_o f(T), \ \ K^* = K_o^* f(T), \ \ D = D_o f(T), \ \ D^* = D_o^* f(T),$$
$$\gamma_1 = \gamma_{1o}f(T)\ , \ \ \gamma_2 = \gamma_{2o}f(T)\ , \ \ f(T) = (1 - \alpha^* T_o)$$

Here λ_{o1}, $\mu_o, K_o, K_o^*, D_o, D_o^*, \gamma_{1o}$ and γ_{2o} are references constants and α^* is an empirical temperature-sensitivity parameter. The temperature-independent case is recovered by setting $f(T) = 1$

3. Solution Procedure

Consider a homogeneous, isotropic thermoelastic-diffusion half-space governed by the Moore–Gibson–Thompson heat-conduction model with temperature-dependent material properties. A Cartesian coordinate system (x_1, x_2, x_3) is adopted such that the plane $x_3 = 0$ defines the boundary and the positive x_3-axis is directed into the medium. The incident and reflected waves are assumed to propagate in the $x_1{}_-x_3$ plane, with the wavefront intersecting the boundary along the x_2-direction.

A plane-strain state is assumed in the $x_1{}_-x_3$ plane; hence, all field variables depend only on $(x_1, x_3$, t).

$$u = (u_1(x_1, x_3, t), 0, u_3(x_1, x_3, t)), P(x_1, x_3, t), \theta(x_1, x_3, t), \tag{3.1}$$

By commuting Eq. (3.1) into Eqs. (2.1), (2.2), (2.3), (2.4), and (2.5), the following set of relation is derived:

$$(\lambda_{o1} + \mu_o)\frac{\partial e}{\partial x_1} + \mu_o\nabla^2 u_1 - \gamma_{1o}\frac{\partial\theta}{\partial x_1} - \gamma_{2o}\frac{\partial P}{\partial x_1} = \frac{\rho(1-\xi^2\nabla^2)}{f(T)}\frac{\partial^2 u_1}{\partial t^2}, \tag{3.2}$$

$$(\lambda_{o1} + \mu_o)\frac{\partial e}{\partial x_3} + \mu_o\nabla^2 u_3 - \gamma_{1o}\frac{\partial\theta}{\partial x_3} - \gamma_{2o}\frac{\partial P}{\partial x_3} = \frac{\rho(1-\xi^2\nabla^2)}{f(T)}\frac{\partial^2 u_3}{\partial t^2}, \tag{3.3}$$

$$f(T)\left(K_o\frac{\partial}{\partial t} + K_o^*\right)\nabla^2\varphi = \left(1 + \tau_o\frac{\partial}{\partial t}\right)\left(T_o l\frac{\partial^2\theta}{\partial t^2} + \gamma_{1o}T_o f(T)\frac{\partial^2 e}{\partial t^2} + dT_o\frac{\partial^2 P}{\partial t^2}\right), \tag{3.4}$$

$$f(T)\left(D_o\frac{\partial}{\partial t} + D_o^*\ \right)\nabla^2 P = \left(1 + \tau_1\frac{\partial}{\partial t}\right)\left(n\frac{\partial^2 P}{\partial t^2} + \gamma_{2o}f(T)\frac{\partial^2 e}{\partial t^2} + d\frac{\partial^2\theta}{\partial t^2}\right), \tag{3.5}$$

$$\ddot{\theta} = \ddot{\varphi} - \beta^*\nabla^2\varphi, \tag{3.6}$$

$$t_{33} = (\lambda_{o1} + 2\mu_0)f(T)u_{3,3} + \lambda_{o1}f(T)u_{1,1} - \gamma_{1o}f(T)\theta - \gamma_{2o}f(T)P, \tag{3.7}$$

$$t_{31} = \mu_0 f(T)\left(\frac{\partial u_1}{\partial x_3} + \frac{\partial u_3}{\partial x_1}\right). \tag{3.8}$$

Where:

$$e = \frac{\partial u_1}{\partial x_1} + \frac{\partial u_3}{\partial x_2}, \nabla^2 = \frac{\partial^2 u_1}{\partial x_1^2} + \frac{\partial^2 u_3}{\partial x_3^2}.$$

Introducing the following dimensionless variables simplifies the governing equations:

$$(x_i', u_i') = \frac{\omega_1^*}{C_1}(x_i, u_i), (t', \tau_o', \tau_1') = \omega_1^*(t, \tau_0, \tau_1), \theta' = \frac{\gamma_{10}}{\rho C_1^2}\theta, P' = \frac{1}{\gamma_{20}b}P, (\theta', \phi') = \frac{\gamma_{1o}}{\rho C_1^2}(\theta, \phi),$$

$(Z_1', Z_2') = \frac{C_1}{\gamma_{10}T_o}(Z_1, Z_2),\ Z_3' = \frac{C_1}{K_o}Z_3,\ Z_4' = \frac{C_1}{D_o}Z_4,\ t_{ij}' = \frac{t_{ij}}{\gamma_{10}T_o}.$ (3.9)

Where:

$\omega_1^* = \frac{\rho C_e C_1^2}{K},\ \ C_1^2 = \frac{\lambda_{o1}+2\mu_o}{\rho}.$

By substituting Eq. (3.9) into Eqs. (3.2), (3.3), (3.4), (3.5), (3.6), (3.7), and (3.8), we obtain:

$$p_{11}\frac{\partial e}{\partial x_1} + p_{12}\nabla^2 u_1 - \frac{\partial \theta}{\partial x_1} - p_{13}\frac{\partial P}{\partial x_1} = \frac{(1-\xi^2\nabla^2)}{f(T)}\frac{\partial^2 u_1}{\partial t^2}, \quad (3.10)$$

$$p_{11}\frac{\partial e}{\partial x_3} + p_{12}\nabla^2 u_3 - \frac{\partial \theta}{\partial x_3} - p_{13}\frac{\partial P}{\partial x_3} = \frac{(1-\xi^2\nabla^2)}{f(T)}\frac{\partial^2 u_3}{\partial t^2}, \quad (3.11)$$

$$f(T)\left(\frac{\partial}{\partial t} + p_{14}\right)\nabla^2\theta = \left(1 + \tau_o\frac{\partial}{\partial t}\right)\left(p_{15}\frac{\partial^2\theta}{\partial t^2} + p_{16}f(T)\frac{\partial^2 e}{\partial t^2} + p_{17}\frac{\partial^2 P}{\partial t^2}\right), \quad (3.12)$$

$$f(T)\left(\frac{\partial}{\partial t} + p_{18}\right)\nabla^2 P = \left(1 + \tau_1\frac{\partial}{\partial t}\right)\left(p_{19}\frac{\partial^2 P}{\partial t^2} + p_{20}f(T)\frac{\partial^2 e}{\partial t^2} + p_{21}\frac{\partial^2\theta}{\partial t^2}\right), \quad (3.13)$$

$$\ddot{\theta} = \ddot{\varphi} - \beta^*\nabla^2\ddot{\varphi}, \quad (3.14)$$

$$t_{33} = p_{23}\frac{\partial u_3}{\partial x_3} + p_{22}\frac{\partial u_1}{\partial x_1} - p_{24}\theta - p_{25}P, \quad (3.15)$$

$$t_{31} = p_{26}\left(\frac{\partial u_1}{\partial x_3} + \frac{\partial u_3}{\partial x_1}\right). \quad (3.16)$$

Where p_i (i=11-27) are listed in Appendix-I.

u_1 & u_3 can be stated in terms of potential functions as:

$$u_1 = \frac{\partial\phi}{\partial x_1} - \frac{\partial\psi}{\partial x_3},\quad u_3 = \frac{\partial\phi}{\partial x_3} + \frac{\partial\psi}{\partial x_1}. \quad (3.17)$$

Substituting Eq. (3.17) into Eqs. (3.10), (3.11), (3.12), (3.13), (3.14), (3.15), and (3.16), we arrive at:

$$\left(\nabla^2 - \frac{(1-\xi^2\nabla^2)}{f(T)}\frac{\partial^2}{\partial t^2}\right)\phi - \theta - c_{13}P = 0, \quad (3.18)$$

$$\left(\nabla^2 - \frac{1(1-\xi^2\nabla^2)}{f(T)}\frac{1}{p_{12}}\frac{\partial^2}{\partial t^2}\right)\psi = 0, \quad (3.19)$$

$$f(T)\left(\frac{\partial}{\partial t} + p_{14}\right)\nabla^2\varphi = \left(1 + \tau_o\frac{\partial}{\partial t}\right)\left(p_{15}\frac{\partial^2\theta}{\partial t^2} + p_{16}f(T)\frac{\partial^2\nabla^2\phi}{\partial t^2} + p_{17}\frac{\partial^2 P}{\partial t^2}\right), \quad (3.20)$$

$$f(T)\left(\frac{\partial}{\partial t} + p_{18}\right)\nabla^2 P = \left(1 + \tau_1\frac{\partial}{\partial t}\right)\left(p_{19}\frac{\partial^2 P}{\partial t^2} + p_{20}f(T)\frac{\partial^2\nabla^2\phi}{\partial t^2} + p_{21}\frac{\partial^2\theta}{\partial t^2}\right), \quad (3.21)$$

$$t_{33} = (p_{23} - p_{22})\frac{\partial^2}{\partial x_1\partial x_3}\psi + p_{23}\frac{\partial^2\phi}{\partial x_3^2} + p_{22}\frac{\partial^2\phi}{\partial x_1^2} - p_{24}\theta - p_{25}P, \quad (3.22)$$

$$t_{31} = 2p_{26}\frac{\partial^2\emptyset}{\partial x_1\partial x_3} + p_{26}\left(\frac{\partial^2}{\partial x_1^2} - \frac{\partial^2}{\partial x_3^2}\right)\psi. \quad (3.23)$$

4. Dispersion Equations and Its Solution

For time-harmonic plane waves propagating in the $x_1 - x_3$ plane, the wave normal makes an angle θ_o with the positive x_3- axis. The field variables satisfying Eqs. (3.18), (3.19), (3.20), and (3.21), are assumed in form:

$$(\phi, \psi, \varphi, P) = (\phi^o, \psi^o, \varphi^o, P^o)e^{ik(x_1 sin\theta_o - x_3 cos\theta_o + \vartheta t)}, \quad (4.1)$$

where $\phi^o, \psi^o, \varphi^o, P^o$ are amplitudes, k is wave number and ϑ is the phase velocity

Substitution of Eq. (4.1) into Eqs. (3.18), (3.19), (3.20), and (3.21), yields

$$(F_{11}\vartheta^6 + F_{12}\vartheta^4 + F_{13}\vartheta^2 + F_{14})(\phi^o, \varphi^o, P^o) = 0, \quad (4.2)$$

$$(\vartheta^2 - f(T)p_{12})\psi^o = 0. \quad (4.3)$$

The roots ϑ_i(i=1, 2, 3) of $F_{11}\vartheta^6 + F_{12}\vartheta^4 + F_{13}\vartheta^2 + F_{14}$=0 correspond to: P-, T-, and P_o--waves, respectively, where $\vartheta_4 = \sqrt{f(T)p_{12}}$ gives the SV-wave velocity. The coefficients F_i (i=11–14) are given in Appendix II.

5. Boundary Constraints

Impedance boundary conditions represent partial interfacial bonding and energy exchange by relating the boundary tractions and fluxes to the corresponding field variables. Following Tiersten [39] and Malischewsky [40], the conditions at $x_3 = 0$ are expressed as:

$$\left.\begin{aligned} t_{33}+\omega Z_1 u_3 &= 0\\ t_{31}+\omega Z_2 u_1 &= 0\\ K_0\frac{\partial \varphi}{\partial x_3}+\omega Z_3\varphi &= 0\\ D_0\frac{\partial P}{\partial x_3}+\omega Z_4 P &= 0 \end{aligned}\right\}. \tag{5.1}$$

Here, Z1 and Z2 are mechanical impedance with units N sec m^{-3}., whereas Z_3 and Z_4 are the thermal and diffusive impedences with units of N $m^{-1}K^{-1}$ and Ns^4m^{-4} *respectively*. Setting Z_1=Z_2= Z_3= Z_4 corresponds to a traction-free surface

6. Reflection of Waves

An incident P-, T-, P_0, or SV-wave striking the boundary at an angle θ_o generates four reflected modes: P, T, P_0, and SV- waves. Their reflection angles $\theta_1, \theta_2, \theta_3$ *and* θ_4 respectively, are measured from the positivex_3 - axis.

Hence, the total field is expressed as the superposition of the incident and reflected waves:

$\phi = \sum_{j=1}^{3}\{F_{oj}e^{ik_j(x_1\sin\theta_o - x_3\cos\theta_o)+i\omega t} + F_j e^{ik_j(x_1\sin\theta_j + x_3\cos\theta_j)+i\omega t}\}$, (6.1)

$\varphi = \sum_{j=1}^{3} r_j\{F_{oj}e^{ik_j(x_1\sin\theta_o - x_3\cos\theta_o)+i\omega t} + F_j e^{ik_j(x_1\sin\theta_j + x_3\cos\theta_j)+i\omega t}\}$, (6.2)

$P = \sum_{j=1}^{3} s_j\{F_{oj}e^{ik_j(x_1\sin\theta_o - x_3\cos\theta_o)+i\omega t} + F_j e^{ik_j(x_1\sin\theta_j + x_3\cos\theta_j)+i\omega t}\}$, (6.3)

$\psi = F_{o4}e^{ik_j(x_1\sin\theta_o - x_3\cos\theta_o)+i\omega t} + F_4 e^{ik_4(x_1\sin\theta_4 + x_3\cos\theta_4)+i\omega t}$. (6.4)

Here, r_j and s_j (j=1, 2, 3) are the coupling coefficients listed in Appendix III. F_{oj}(j=1,2,3) and F_{o4} denote the amplitudes of the incident wave P-, T-, $P_o -$ and SV- waves, respectively, while F_j(j=1, 2, 3) and F_4 represent the corresponding reflected wave-amplitudes. The incidence and reflection angles satisfy Snell's law:

$$\frac{\sin\theta_o}{v_o} = \frac{\sin\theta_j}{v_j}$$

Where:

$k_j v_j = \omega$, at $x_3 = 0$ (j= 1 … 4)

$$v_0 = \begin{cases} v_1, & P(incident),\\ v_2, & T(incident),\\ v_3, & P_o(incident),\\ v_4, & SV(incident). \end{cases} \tag{6.5}$$

Here v_0 and v_i denote the phase velocities of the incident and reflected waves, respectively. Substitution of Eqs. (6.1), (6.2), (6.3), and (6.4) and Eq. (3.14) into the boundary conditions Eq. (5.1), together with Eqs. (3.22) and (3.23), gives:

$\sum_{i,j=1}^{4} C_{ij}R_j = Y_j$. (6.6)

The coefficient matrices C_{ij}, amplitude ratios R_j, and forcing vector Y_j are defined in Appendix IV.

7. Particular Cases:

i) Absence of temperature dependent parameters:

The temperature-independent case is obtained by setting α* = 0 in equation (38), yield the corresponding results for thermoelastic diffusion with HTT and MGT model.

ii) Diffusion-Free:

The diffusion-free model follows from $\beta_2 = a = D_0 = D_0^* = n = 0$, reducing the system to coupled thermoelasticity with mechanical and thermal impedance conditions, as summarized in Appendix V.

iii) Elastic–Diffusive:

The elastic-diffusive model is recovered by suppressing the thermal field and its coupling parameters, ($\beta_1 = c_e = c_b = K_0 = K_0^* = 0$), leaving only mechanical and diffusive boundary contributions; the corresponding system is given in Appendix VI.

iv) Stress-Free Surface Condition:

Setting $Z_1 = Z_2 = Z_3 = Z_4 = 0$ yields the zero-impedance limit, comprising traction-free, thermally insulated, and diffusion-impermeable boundary conditions, with the resulting algebraic system listed in Appendix VII.

8. Computational Results and Interpretation:

Following Dhaliwal and Singh [38], the material parameters used in the numerical computations are taken as:

$\lambda_{01} = 2.696\times10^{10}Kgm^{-1}s^{-2}$, $\mu_0 = 1.639\times10^{10}Kgm^{-1}$, $\rho = 1.74\times10^{3}Kgm^{-3}$,

$T_0 = 0.293K, \quad c_e = 1.04 \times 10^3 JKg^{-1},$
$\alpha_T = .0178 \times 10^{-5} K^{-1}, \alpha_C = .0198 \times 10^{-4} Kg^{-1}m^3,$
$a = 1.02 \times 10^4 m^2K^{-1}s^{-2}, b = 9 \times 10^5 Kg^{-1}m^5s^{-2}, \ K_0 = 1.7 \times 10^2 Wm^{-1}K^{-1},$
$K_o^* = 1.4W/mks, D_o = 0.85 \times 10^{-8} Kgm^{-3}s, \ \ D_o^* = 0.65Kgsm^{-3}, \omega = 1.$
$\tau_o = 0.002sec, \tau_1 = 0.004sec,$

For Figs. 1(a, b, c, d), 2(a, b, c, d), and 3(a, b, c, d),, α* = 0.3 and (Z_1, Z_2, Z_3, Z_4) = (10, 20, 30, 40). The solid, dotted, and dashed curves denote the HTT-MGT model with ζ* = 0.2, the 2TT-MGT model with ζ* = 0.6, and the HTT-MGT model with ζ* = 0, respectively. For Figs. 4(a, b, c, d), 5(a, b, c, d), and 6(a, b, c, d), the solid and dotted curves represent the MGT and Lord-Shulman models with (Z_1, Z_2, Z_3, Z_4) = (10, 20, 30, 40), whereas the dashed curve denotes the MGT model without impedance, $Z_1 = Z_2 = Z_3 = Z_4 = 0$. For Figs. 7(a, b, c, d), 8(a, b, c, d), and 9(a, b, c, d), the solid, dotted, and dashed curves correspond to α* = 0.2, 0.4, and 0, respectively. For Figs. 10(a, b, c, d), 11(a, b, c, d), and 12(a, b, c, d), the solid, dotted, and dashed curves correspond to ξ = 0.2, 0.4, and 0, respectively.

I. Effect of Hyperbolic Two Temperature (HTT).

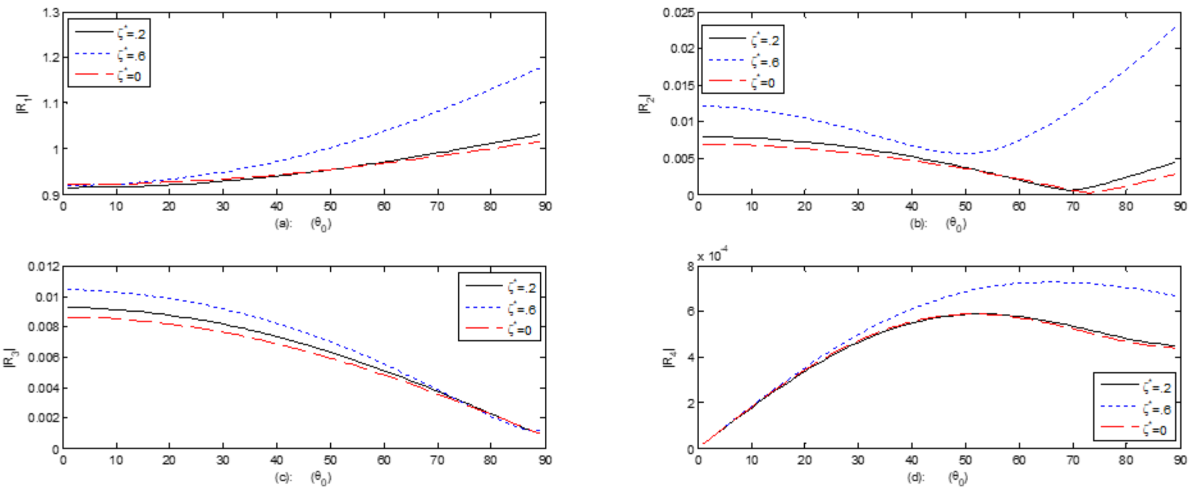

Fig. 1 (a, b, c, d): HTT effects on amplitude ratios for an incident P -wave.

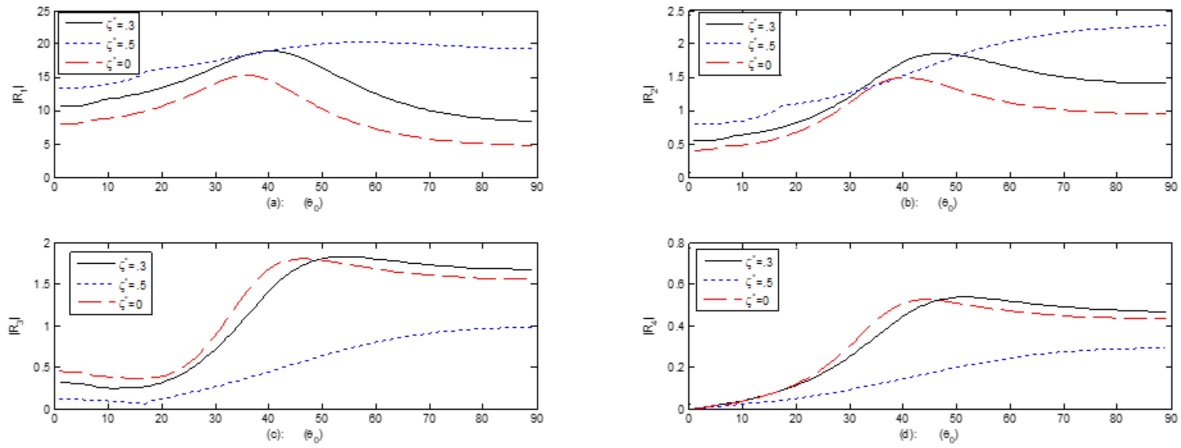

Fig. 2 (a, b, c, d): HTT effects on amplitude ratios for an incident T -wave.

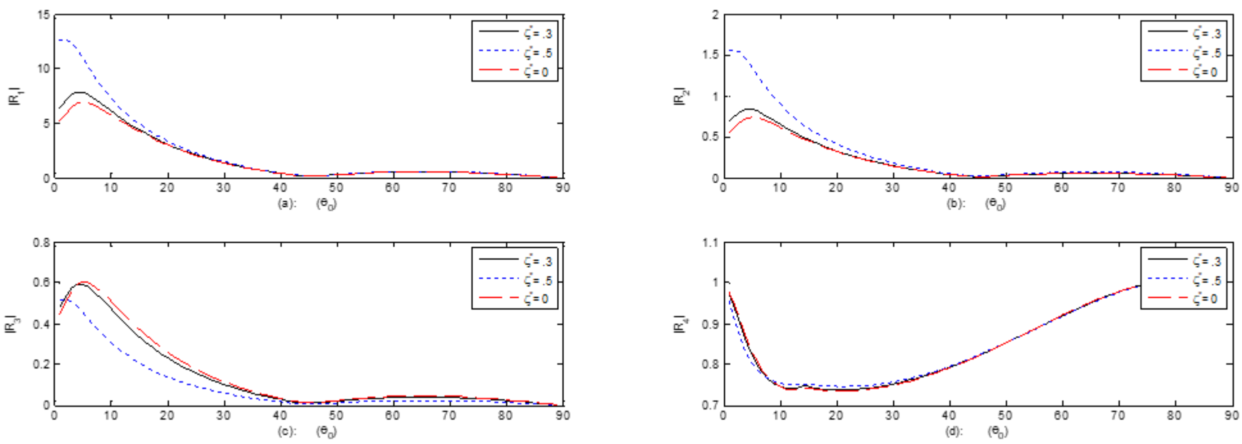

Fig. 3 (a, b, c, d): HTT effects on amplitude ratios for an incident SV -wave

Fig. 1(a) illustrates the variation of $|R_1|$ with the incidence angle θ_0. The amplitude ratio $|R_1|$ for the HTT, 2TT, and 1T cases increases with θ_0, although the magnitudes remain distinct. Among these cases, the 2TT model gives the largest $|R_1|$, indicating stronger reflection of the P-wave component. Fig. 1(b) shows the variation of $|R_2|$ with θ_0. The amplitude ratio $|R_2|$ for the HTT and 1T cases decreases up to about 70° and then increases slightly, whereas $|R_2|$ for the 2TT case displays a similar decline followed by a more pronounced recovery near grazing incidence. Fig. 1(c) presents the variation of $|R_3|$ with θ_0. The amplitude ratio $|R_3|$ for the HTT, 2TT, and 1T cases decreases throughout most of the angular range and approaches its minimum at larger incidence angles. The relatively small separation among the three responses indicates weak sensitivity of $|R_3|$ to the thermal model. Figure 2(d) depicts the variation of $|R_4|$ with θ_0. The amplitude ratio $|R_4|$ for the HTT and 1T cases increases up to nearly 50° and then decreases, while $|R_4|$ for the 2TT case continues to increase up to about 65° before declining. Fig. 2(a) illustrates the variation of $|R_1|$ with θ_0. The amplitude ratio $|R_1|$ for the HTT and 1T cases increases up to approximately 40° and then decreases, whereas $|R_1|$ for the 2TT case rises more gradually and reaches a broader maximum. Fig. 2(b) shows the variation of $|R_2|$ with θ_0. The amplitude ratio $|R_2|$ for the HTT and 1T cases increases to a peak near 41° and subsequently decreases. In contrast, $|R_2|$ for the 2TT case attains a larger and more sustained magnitude over the angular range. Fig. 2(c) presents the variation of $|R_3|$ with θ_0. The amplitude ratio $|R_3|$ for the HTT and 1T cases initially decreases, increases between nearly 16° and 45°, and then decreases again. The 2TT value of $|R_3|$ increases almost monotonically, demonstrating stronger sensitivity of the diffusive mode to the two-temperature effect. Fig. 2(d) depicts the variation of $|R_4|$ with θ_0. The amplitude ratio $|R_4|$ for the HTT and 1T cases increases up to about 42° and then decreases, whereas $|R_4|$ for the 2TT case increases more steadily with θ_0. Fig. 3(a) illustrates the variation of $|R_1|$ with θ_0. The amplitude ratio $|R_1|$ for the HTT, 2TT, and 1T cases initially increases, with the 2TT case producing the highest low-angle peak. It then decreases up to nearly 45°, rises again between about 45° and 65°, and finally declines. Fig. 3(b) shows the variation of $|R_2|$ with θ_0. The amplitude ratio $|R_2|$ for the HTT and 1T cases increases at small angles, decreases over the intermediate range, and rises again before falling at larger angles. The value of $|R_2|$ for the 2TT case decreases up to about 45° and then increases. Fig. 3(c) presents the variation of $|R_3|$ with θ_0. The amplitude ratio $|R_3|$ for the HTT, 2TT, and 1T cases follows a common pattern of initial growth, intermediate attenuation, secondary amplification between approximately 45° and 65°, and final decay. Fig. 3(d) depicts the variation of $|R_4|$ with θ_0. The amplitude ratio $|R_4|$ for the HTT, 2TT, and 1T cases decreases up to nearly 23° and then increases markedly, indicating recovery of the reflected SV-wave amplitude at higher incidence angles.

II. Effect of Impedance parameter:

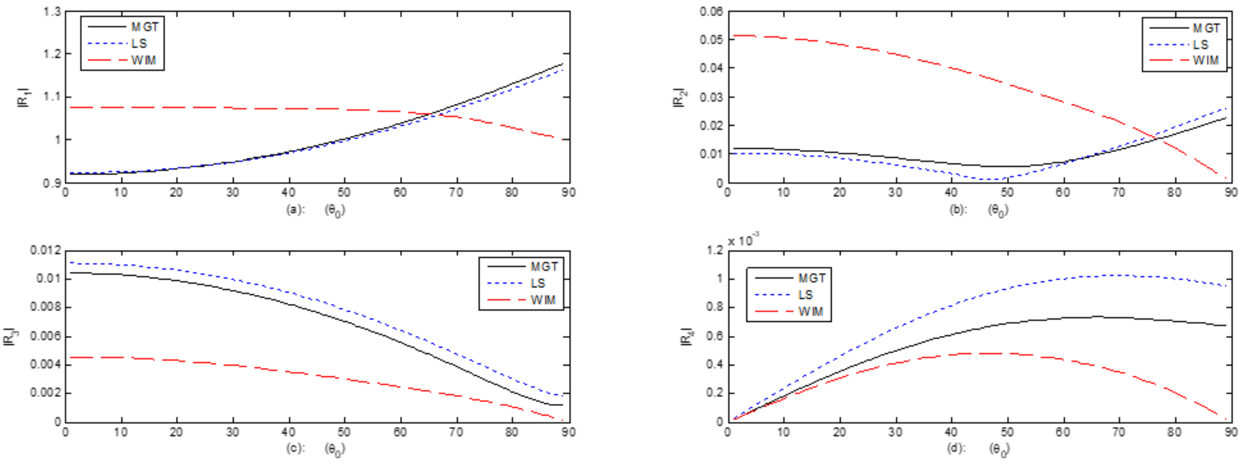

Fig. 4 (a, b, c, d): Impedance and thermoelastic-model effects on amplitude ratios for an incident P-wave.

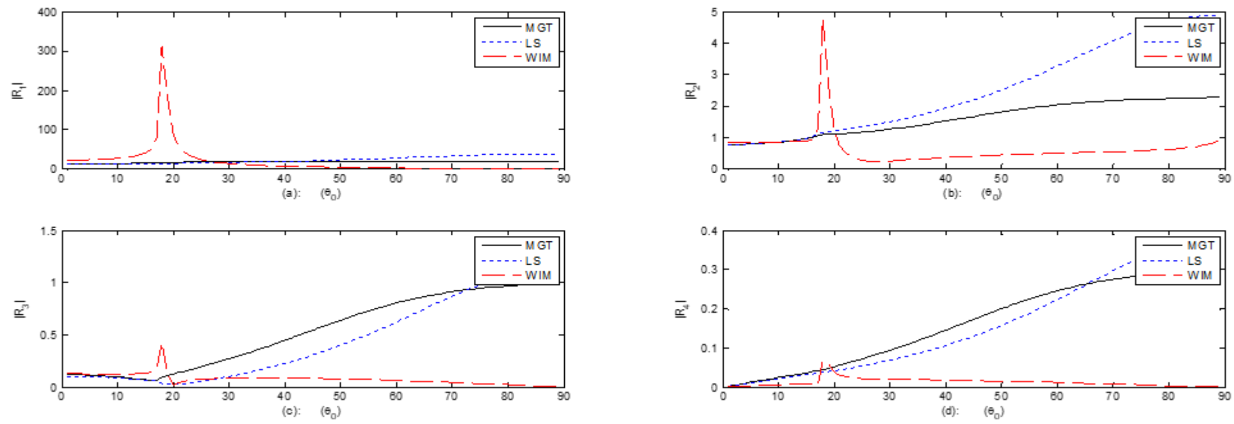

Fig. 5 (a, b, c, d): Impedance and thermoelastic-model effects on amplitude ratios for an incident T -wave.

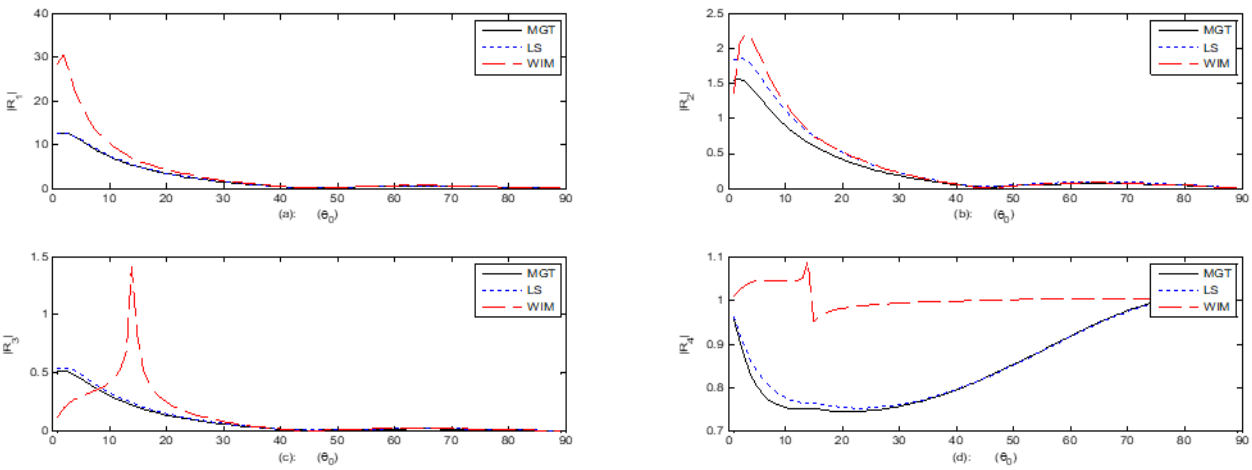

Fig. 6 (a, b, c, d): Impedance and thermoelastic-model effects on amplitude ratios for an incident SV -wave.

Fig. 4(a) illustrates the variation of $|R_1|$ with θ_0. The amplitude ratio $|R_1|$ for the MGT and LS cases with impedance increases slightly, whereas $|R_1|$ for the WIM case decreases gradually. This contrast shows that impedance sustains the reflected P-wave amplitude. Fig. 4(b) shows the variation of $|R_2|$ with θ_0. The amplitude ratio $|R_2|$ for the MGT and LS cases decreases up to about 55° and then increases, while $|R_2|$ for the WIM case decreases almost monotonically. Fig. 4(c) presents the variation of $|R_3|$ with θ_0. The amplitude ratio $|R_3|$ for the MGT, LS, and WIM cases decreases with increasing θ_0, although the three cases retain noticeably different magnitudes. Fig. 4(d) depicts the variation of $|R_4|$ with θ_0. The amplitude ratio $|R_4|$ for the MGT and LS cases increases up to nearly 65° and then decreases, whereas $|R_4|$ for the WIM case exhibits a more irregular angular response. Fig. 5(a) illustrates the variation of $|R_1|$ with θ_0. The amplitude ratio $|R_1|$ for the MGT and LS cases increases gradually, while $|R_1|$ for the WIM case increases only up to about 18° and then decreases. Fig. 5(b) shows the variation of $|R_2|$ with θ_0. The amplitude ratio $|R_2|$ for the MGT and LS cases increases over most of the angular range, with the LS case attaining the largest values. The WIM value of $|R_2|$ reaches an early peak and subsequently declines. Fig. 5(c) presents the variation of $|R_3|$ with θ_0. The amplitude ratio $|R_3|$ for the MGT and LS cases increases toward pronounced maxima, whereas $|R_3|$ for the WIM case rises only up to approximately 20° before decreasing. Fig. 5(d) depicts the variation of $|R_4|$ with θ_0. The amplitude ratio $|R_4|$ for the MGT and LS cases remains enhanced over a broad angular interval, while $|R_4|$ for the WIM case reaches a low-angle maximum and then attenuates. Fig. 6(a) illustrates the variation of $|R_1|$ with θ_0. The amplitude ratio $|R_1|$ for the MGT, LS, and WIM cases decreases monotonically, indicating limited sensitivity of the primary reflected mode to the boundary model. Fig. 6(b) shows the variation of $|R_2|$ with θ_0. The amplitude ratio $|R_2|$ for the MGT, LS, and WIM cases increases slightly at very small angles, decreases between about 3° and 45°, and then rises again at larger angles. Fig. 6(c) presents the variation of $|R_3|$ with θ_0. The amplitude ratio $|R_3|$ for the MGT and LS cases decreases smoothly, whereas $|R_3|$ for the WIM case initially increases, reaches a peak near 13°, and then decreases. Fig. 6(d) depicts the variation of $|R_4|$ with θ_0. The amplitude ratio $|R_4|$ for the MGT and LS cases decreases up to approximately 24° and then increases, while $|R_4|$ for the WIM case exhibits an additional local rise and fall before increasing again.

III. Effect of temperature dependent property (TDP).

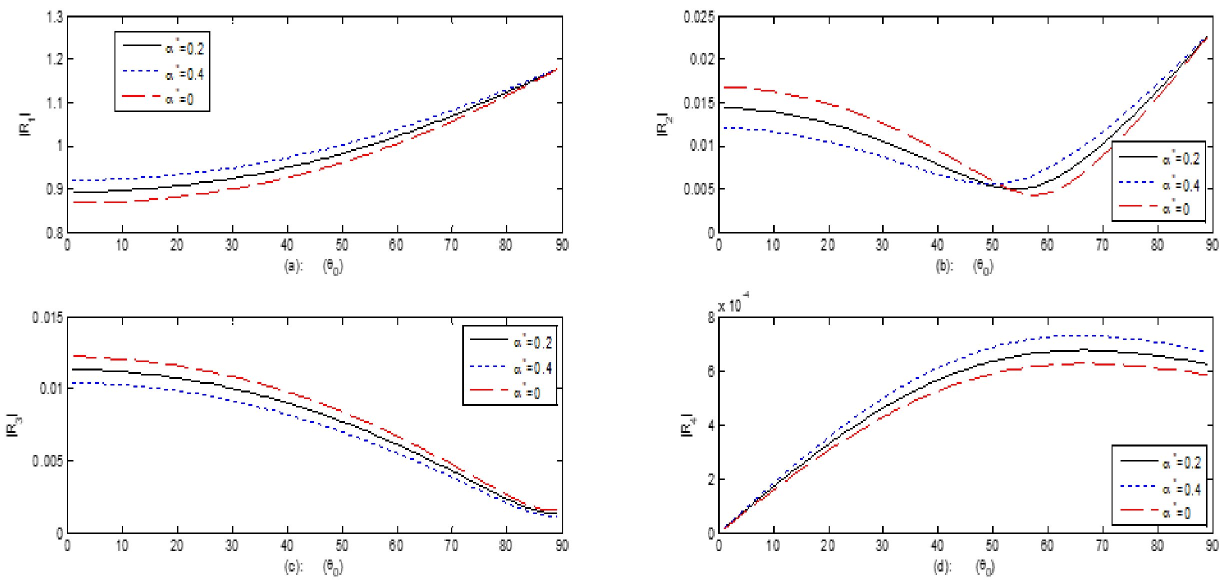

Fig. 7 (a, b, c, d): TDP effects on amplitude ratios for an incident P-wave.

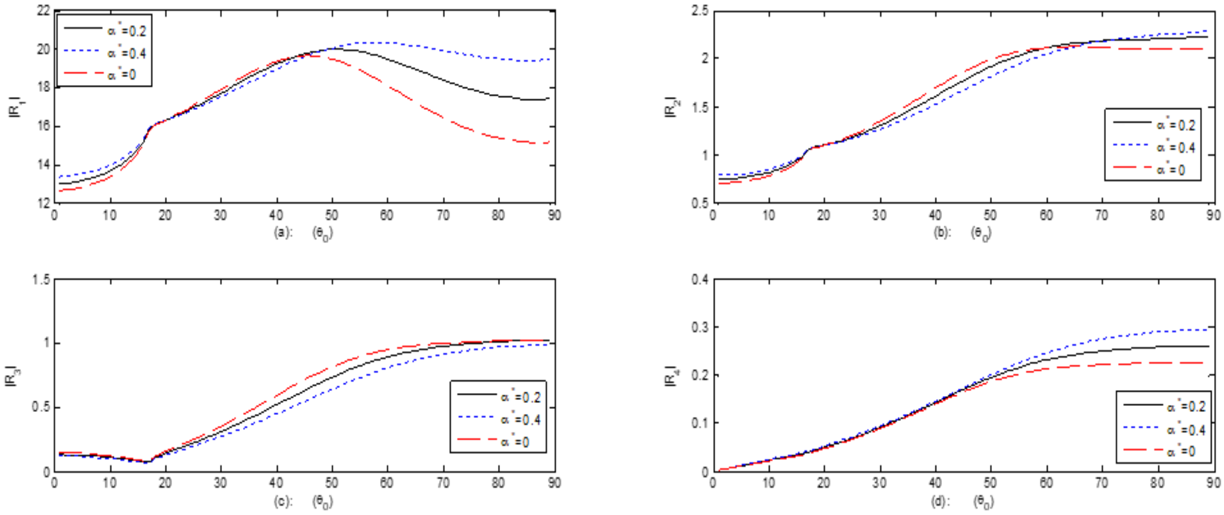

Fig. 8 (a, b, c, d): TDP effects on amplitude ratios for an incident T -wave.

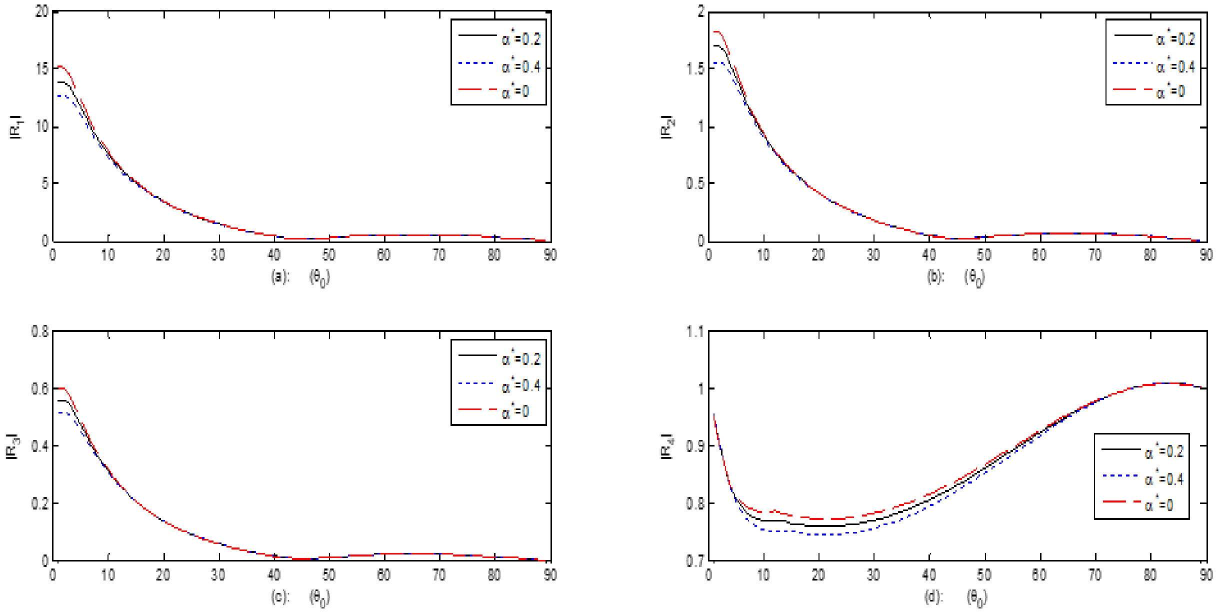

Fig. 9 (a, b, c, d): TDP effects on amplitude ratios for an incident SV -wave.

Fig. 7(a) illustrates the variation of $|R_1|$ with θ_0. The amplitude ratio $|R_1|$ for $\alpha^* = 0$, 0.2, and 0.4 increases steadily over the complete angular range. The three responses follow nearly parallel trends, with a clear separation in magnitude. Fig. 7(b) shows the variation of $|R_2|$ with θ_0. The amplitude ratio $|R_2|$ for $\alpha^* = 0$, 0.2, and 0.4 decreases up to about 55°, where a minimum is observed, and then rises slightly toward grazing incidence. The ordering of the three cases remains distinct throughout the range. Fig. 7(c) presents the variation of $|R_3|$ with θ_0. The amplitude ratio $|R_3|$ for $\alpha^* = 0$, 0.2, and 0.4 decreases continuously as θ_0 increases. No change in the overall trend is observed, although the amplitudes differ among the three parameter values. Fig. 7(d) depicts the variation of $|R_4|$ with θ_0. The amplitude ratio $|R_4|$ for $\alpha^* = 0$, 0.2, and 0.4 increases up to nearly 68°, reaches a maximum, and then decreases at higher incidence angles. The peak magnitudes differ for the three cases Fig. 8(a) illustrates the variation of $|R_1|$ with θ_0. The amplitude ratio $|R_1|$ for $\alpha^* = 0$, 0.2, and 0.4 increases throughout most of the angular range. The three cases show similar profiles, with moderate differences in magnitude. Fig. 8(b) shows the variation of $|R_2|$ with θ_0. The amplitude ratio $|R_2|$ for $\alpha^* = 0$, 0.2, and 0.4 increases as θ_0 advances. Among the considered cases, $\alpha^* = 0.4$ produces the largest amplitude over most of the range. Fig. 8(c) presents the variation of $|R_3|$ with θ_0. The amplitude ratio $|R_3|$ for $\alpha^* = 0$, 0.2, and 0.4 decreases up to about 18° and then increases gradually. The minimum occurs at approximately the same angle for all three cases. Fig. 8(d) depicts the variation of $|R_4|$ with θ_0. The amplitude ratio $|R_4|$ for $\alpha^* = 0$, 0.2, and 0.4 increases over the entire angular range. The responses remain separated, with different magnitudes for the three values of α^*. Fig. 9(a) illustrates the variation of $|R_1|$ with θ_0. The amplitude ratio $|R_1|$ for $\alpha^* = 0$, 0.2, and 0.4 decreases up to about 45°, rises between approximately 45° and 65°, and then decreases again. The three responses exhibit the same sequence of variation. Fig. 9(b) shows the variation of $|R_2|$ with θ_0. The amplitude ratio $|R_2|$ for $\alpha^* = 0$, 0.2, and 0.4 decreases in the low- and intermediate-angle ranges, increases between about 45° and 65°, and declines thereafter. The main turning points occur at nearly the same angles. Fig. 9(c) presents the variation of $|R_3|$ with θ_0. The amplitude ratio $|R_3|$ for $\alpha^* = 0$, 0.2, and 0.4 follows a decrease–increase–decrease pattern. A secondary rise is observed over the 45°–65° interval before the amplitude falls near grazing incidence. Fig. 9(d) depicts the variation of $|R_4|$ with θ_0. The amplitude ratio $|R_4|$ for $\alpha^* = 0$, 0.2, and 0.4 decreases up to nearly 23° and then increases with θ_0. The minimum occurs in the low-angle region for all three cases.

IV. Effect of Non-local parameters

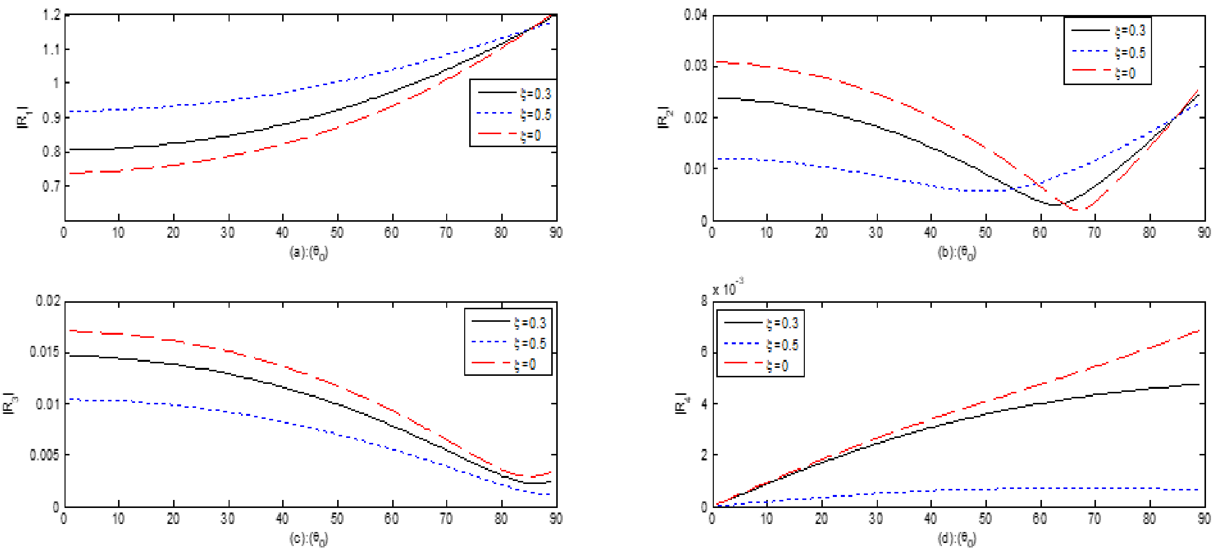

Fig. 10 (a, b, c, d): Nonlocal influence on amplitude ratios for an incident P-wave.

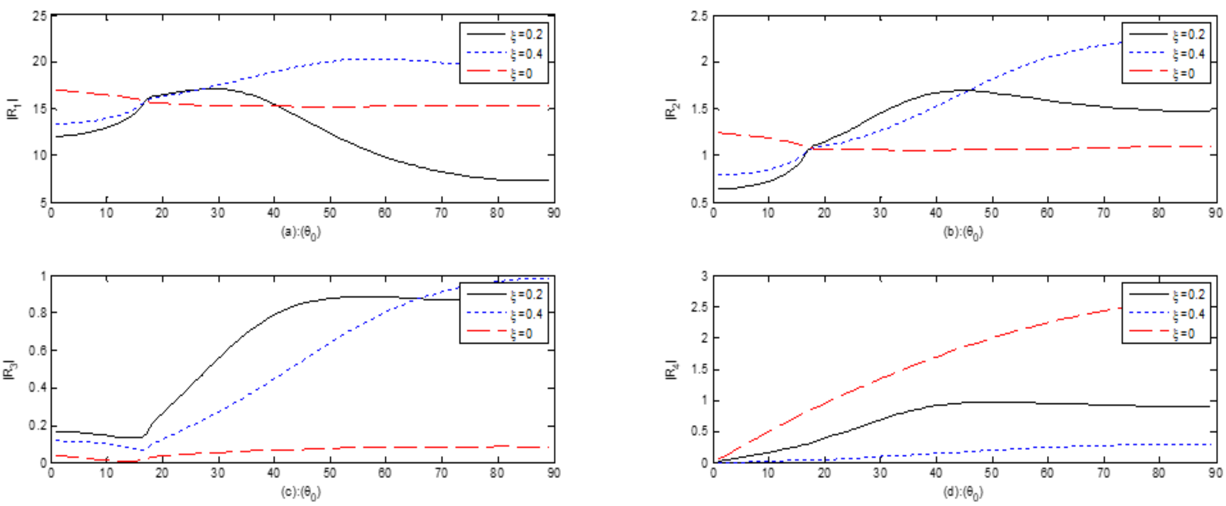

Fig. 11 (a, b, c, d): Nonlocal influence on amplitude ratios for an incident T -wave.

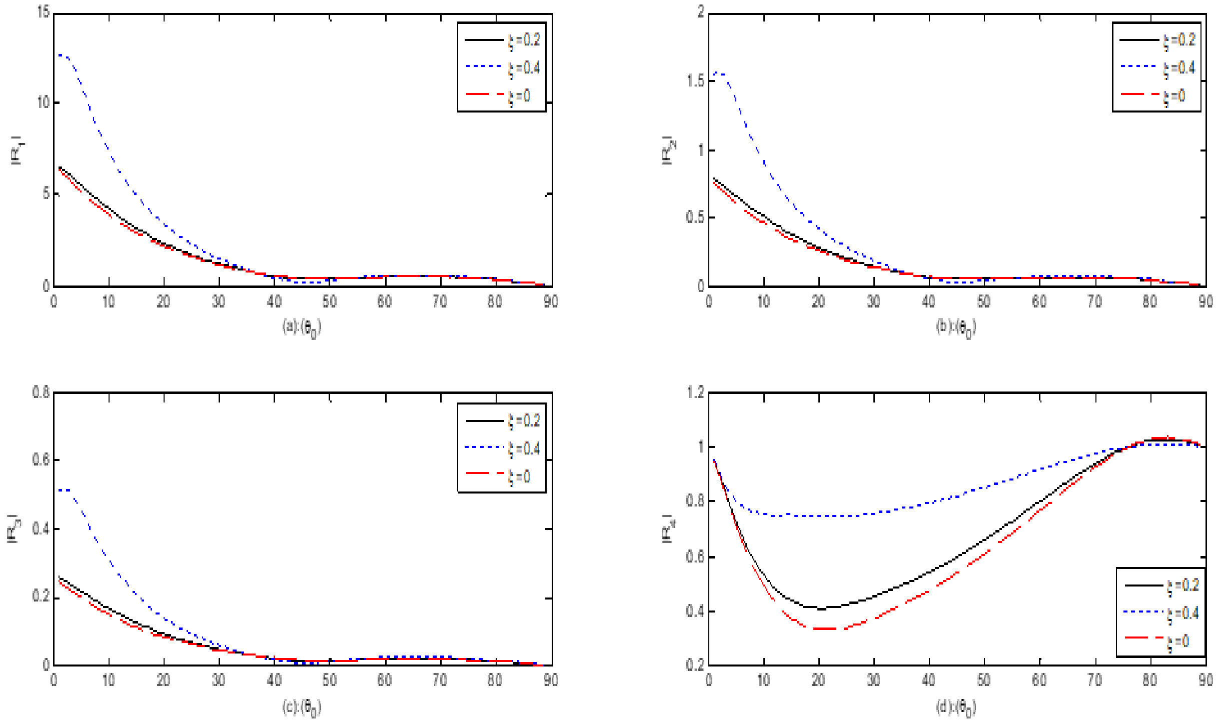

Fig. 12 (a, b, c, d): Nonlocal influence on amplitude ratios for an incident SV -wave.

Fig. 10(a) illustrates the variation of $|R_1|$ with θ_0. The amplitude ratio $|R_1|$ for $\xi = 0$, 0.2, and 0.4 increases with θ_0, while the three cases remain clearly separated in magnitude. The largest difference among the responses is observed at higher incidence angles. Fig. 10(b) shows the variation of $|R_2|$ with θ_0. The amplitude ratio $|R_2|$ for $\xi = 0$, 0.2, and 0.4 decreases over most of the angular range and reaches a minimum before rising near grazing incidence. The recovery occurs at slightly different levels for the three values of ξ. Fig. 10(c) presents the variation of $|R_3|$ with θ_0. The amplitude ratio $|R_3|$ for $\xi = 0$, 0.2, and 0.4 decreases monotonically throughout the considered range. Although the overall pattern is similar, the magnitude of $|R_3|$ changes appreciably with ξ. Fig. 10(d) depicts the variation of $|R_4|$ with θ_0. The amplitude ratio $|R_4|$ for $\xi = 0$ and 0.2 increases and approaches a nearly constant value at high angles, whereas $|R_4|$ for $\xi = 0.4$ continues to rise up to about 72° before decreasing slightly. The peak for $\xi = 0.4$ is therefore shifted toward the grazing-incidence region. Fig. 11(a) illustrates the variation of $|R_1|$ with θ_0. The amplitude ratio $|R_1|$ for $\xi = 0.2$ increases up to about 29° and then decreases, while $|R_1|$ for $\xi = 0.4$ continues to rise up to nearly 60° before declining. In contrast, $|R_1|$ for $\xi = 0$ generally decreases over the angular range. Fig. 11(b) shows the variation of $|R_2|$ with θ_0. The amplitude ratio $|R_2|$ for $\xi = 0$ decreases, whereas $|R_2|$ for $\xi = 0.4$ increases with θ_0. For $\xi = 0.2$, $|R_2|$ reaches an intermediate-angle maximum and then falls, giving a trend between the other two cases. Fig. 11(c) presents the variation of $|R_3|$ with θ_0. The amplitude ratio $|R_3|$ for $\xi = 0.2$ and 0.4 decreases initially and then recovers as θ_0 increases, whereas $|R_3|$ for $\xi = 0$ rises more steadily. The turning points for the nonlocal cases occur in the low-to-intermediate angular range. Fig. 11(d) depicts the variation of $|R_4|$ with θ_0. The amplitude ratio $|R_4|$ for $\xi = 0.2$ increases up to about 50° and then decreases, while $|R_4|$ for $\xi = 0$ attains the largest value at high angles. The $\xi = 0.4$ response varies more gradually and remains below the local case near grazing incidence. Fig. 12(a) illustrates the variation of $|R_1|$ with θ_0. The amplitude ratio $|R_1|$ for $\xi = 0$, 0.2, and 0.4 decreases initially, rises between approximately 45° and 64°, and then decreases again. The three cases exhibit similar turning points but different amplitude levels. Fig. 12(b) shows the variation of $|R_2|$ with θ_0. The amplitude ratio $|R_2|$ for $\xi = 0$, 0.2, and 0.4 follows a common decrease-recovery-decrease pattern. The separation among the responses becomes more noticeable in the intermediate-angle region. Fig. 12(c) presents the variation of $|R_3|$ with θ_0. The amplitude ratio $|R_3|$ for $\xi = 0$, 0.2, and 0.4 decreases at low angles, rises over the intermediate-to-high angular range, and then declines near grazing incidence. The secondary maxima occur within nearly the same angular interval for all three cases. Fig. 12(d) depicts the variation of $|R_4|$ with θ_0. The amplitude ratio $|R_4|$ for $\xi = 0$, 0.2, and 0.4 exhibits oscillatory behavior over the full range of θ_0. The values of ξ change both the heights of the local peaks and the angles at which they occur.

9. Conclusion

This study examined plane-wave reflection from a homogeneous, isotropic thermoelastic-diffusion half-space governed by the Moore–Gibson–Thompson heat-conduction model. The formulation incorporates hyperbolic two-temperature effects, temperature-dependent material properties, nonlocality, initial stress, and mechanical, thermal, and diffusive impedance conditions. The coupled dispersion relation yields reflected P-, thermal, diffusive, and SV-wave modes, whose amplitude ratios were obtained from the boundary system.

The numerical results show that the reflected amplitudes depend strongly on the angle of incidence and the selected constitutive and boundary parameters. The HTT, 2TT, and one-temperature models produce distinct amplitude levels and turning points, particularly for the converted thermal, diffusive, and SV modes. Impedance conditions substantially modify the angular variation of the reflected amplitudes compared with the zero-impedance case. Temperature-dependent properties mainly affect the magnitude of the amplitude ratios while generally preserving their overall angular trends. Nonlocality produces more pronounced changes in the position and magnitude of local extrema, especially for T- and SV-wave incidence.

The limiting cases recover the temperature-independent, diffusion-free, elastic-diffusive, and zero-impedance models, confirming the consistency of the formulation. The results have potential applications in ultrasonic and seismic characterization of thermally sensitive diffusive solids. Future work may extend the model to layered anisotropic media, with applications in detecting thermal damage, residual stress, and interfacial defects.

Appendix-I

$$p_{11} = \frac{\lambda_{o1}+\mu_o}{(\lambda_{o1}+2\mu_o)}, \quad p_{12} = \frac{\mu_o}{(\lambda_{o1}+2\mu_o)}, \quad p_{13} = \frac{\gamma_{2o}^2 b}{(\lambda_{o1}+2\mu_o)}, \quad p_{14} = \frac{K_o^*}{K_o\omega_1^*}, \quad p_{15} = \frac{T_o l C_1^2}{K_o\omega_1^*}, \quad p_{16} = \frac{\gamma_{1o}^2 T_o}{K_o\omega_1^*\rho}, p_{17} = \frac{dT_o\gamma_{1o}\gamma_{2o}b}{K_o\omega_1^*\rho},$$

$$p_{18} = \frac{D^*}{D\omega_1^*}, \quad p_{19} = \frac{nC_1^2}{D\omega_1^*}, \quad p_{20} = \frac{C_1^2}{D\omega_1^* b}, \quad p_{21} = \frac{dC_1^4\rho}{D\omega_1^*\gamma_{1o}\gamma_{2o}b}, \quad p_{22} = \frac{\lambda_{o1}}{T_o\gamma_{1o}}f(T), \ p_{23} = \frac{\lambda_{o1}+2\mu_o}{T_o\gamma_{1o}}f(T),$$

$$p_{24} = \frac{\rho c_1^2}{T_o\gamma_{1o}}f(T), \quad p_{25} = \frac{\gamma_{2o}^2 b}{T_o\gamma_{1o}}f(T), \quad p_{26} = \frac{\mu_o}{T_o\gamma_{1o}}f(T).$$

Appendix-II

$$D_{10} = 1 + i\omega\tau_o, \ D_{11} = -D_{10}p_{16}f(T), \ D_{12} = D_{10}p_{15}(1-\zeta^*K^2), D_{13} = (i\omega + p_{14})f(T), D_{14} = D_{10}p_{17},$$

$$D_{20} = 1 + \tau_1 i\omega, \ D_{21} = -D_{20}p_{21}f(T), D_{22} = D_{20}p_{21}(1-\zeta^*K^2), \ D_{23} = D_{20}p_{19}, \ D_{24} = (i\omega + p_{18})f(T),$$

$$F_{11} = D_{12}D_{23} - D_{14}D_{22}\left(\frac{1-\xi^2\mathrm{k}^2}{f(T)}\right),$$

$$F_{12} = (D_{12}D_{24} - D_{13}D_{23})(1-\xi^2\mathrm{k}^2) - D_{12}D_{23}f(T)(1-\zeta^*K^2) + D_{14}D_{22}f(T) + D_{11}D_{23}f(T) - D_{14}D_{21}f(T)(1-\zeta^*K^2) - p_{13}D_{11}D_{22}f(T) + p_{13}D_{12}D_{21}\,f(T),$$

$$F_{13} = D_{13}D_{24}(1-\xi^2\mathrm{k}^2) + D_{12}D_{24}f(T) + D_{13}D_{23}f(T) - [D_{11}D_{24}(1-\zeta^*K^2) + p_{13}D_{13}D_{21}]f^2(T), \quad F_{14} = -D_{13}D_{24}f^2(T)$$

$$\zeta^* = \begin{cases} \dfrac{\beta^*}{\omega^2} & \text{for hyperbolic two-temperature (HTT)} \\ a^2 & \text{for two-temperature (2TT)} \\ 0 & \text{for one temperature (1T)} \end{cases},$$

Appendix-III

$r_j = -\frac{(D_{11}D_{23}-D_{14}D_{21})\omega^2\vartheta^2-D_{11}D_{24}\omega^2}{(D_{12}\vartheta^2-D_{13})(D_{23}\vartheta^2-D_{24})-D_{14}D_{22}\vartheta^4}$, $s_j = \frac{(D_{11}D_{22}-D_{12}D_{21})\omega^2\vartheta^2+D_{13}D_{21}\omega^2}{(D_{12}\vartheta^2-D_{13})(D_{23}\vartheta^2-D_{24})-D_{14}D_{22}\vartheta^4}$.

Appendix-IV

$C_{1j} = -p_{23}k_j^2cos^2\theta_j - p_{22}k_j^2sin^2\theta_j - p_{24}r_j - p_{25}s_j + i\omega k_jZ_1cos\theta_j$, $C_{14} = -(p_{23} - p_{22})k_4^2sin\theta_4cos\theta_4 + i\omega k_4Z_1cos\theta_4$

$C_{2j} = -2p_{26}k_j^2sin\theta_jcos\theta_j + i\omega k_jZ_2sin\theta_j$, $C_{24} = -p_{26}k_4^2sin^2\theta_4 + p_{26}k_4^2cos^2\theta_4 - iZ_2\omega k_4cos\theta_4$,

$C_{3j} = ir_jk_j \cos\theta_j + \omega Z_3r_j$, $C_{34} = 0$, $C_{4j} = is_jk_j \cos\theta_j + \omega Z_4s_j$, $C_{44} = 0$, (j=1, 2,

Where R_1, R_2, R_3 and R_4 are the amplitude ratios of reflected P-wave, reflected T-wave, P_o −wave and SV-wave.

$R_1 = \frac{F_1}{F^*}$, $R_2 = \frac{F_2}{F^*}$, $R_3 = \frac{F_3}{F^*}$ and $R_4 = \frac{F_4}{F^*}$.

For incident P-Wave:

$F^* = F_{01}, = F_{02} = F_{03} = F_{04} = 0, Y_1 = p_{23}k_1^2cos^2\theta_O + p_{22}k_1^2sin^2\theta_O + p_{24}r_1 + p_{25}s_1 + i\omega k_1Z_1cos\theta_O$,

$Y_2 = -2c_{26}k_1^2sin\theta_Ocos\theta_O - i\omega k_1Z_2sin\theta_O$, $Y_3 = ir_1k_1 \cos\theta_O - \omega Z_3r_1$, $Y_4 = is_1k_1 \cos\theta_O - \omega Z_4s_1$.

For incident T- wave:

$F^* = F_{02}$, $F_{01} = F_{03} = F_{04} = 0, Y_1 = p_{23}k_2^2cos^2\theta_O + p_{22}k_2^2sin^2\theta_O + p_{24}r_2 + p_{25}s_2 + i\omega k_2Z_1cos\theta_O$,

$Y_2 = -2p_{26}k_2^2sin\theta_Ocos\theta_O - i\omega k_2Z_2sin\theta_O$, $Y_3 = ir_2k_2 \cos\theta_O - \omega Z_3r_2$, $Y_4 = is_2k_2 \cos\theta_O - \omega Z_4s_2$.

For incident P_o − Wave:

$F^* = F_{03}$, $F_{01} = F_{02} = F_{04} = 0, Y_1 = p_{23}k_3^2cos^2\theta_O + p_{22}k_3^2sin^2\theta_O + p_{24}r_3 + p_{25}s_3 + i\omega k_3Z_1cos\theta_O$,

$Y_2 = -2p_{26}k_3^2sin\theta_Ocos\theta_O - i\omega k_3Z_2sin\theta_O, Y_3 = ir_3k_3 \cos\theta_O - \omega Z_3r_3 , Y_4 = is_3k_3 \cos\theta_O - \omega Z_4s_3$.

For incident SV-Wave:

$F^* = F_{04}$, $F_{01} = F_{02} = F_{03} = 0, Y_1 = -(p_{23} - p_{22})k_4^2sin\theta_Ocos\theta_O - i\omega k_4Z_1sin\theta_O$,

$Y_2 = p_{26}k_4^2sin^2\theta_O - p_{26}k_4^2cos^2\theta_O + i\omega k_4Z_2cos\theta_O, Y_3 = 0, Y_4 = 0$.

Appendix-V

$C_{1j}^O = -k_j^2\left(p_{23}cos^2\theta_j + p_{22}sin^2\theta_j\right) - p_{24}r_j + i\omega k_jZ_1cos\theta_j$, $C_{13}^O = -(p_{23} - p_{22})k_4^2sin\theta_4cos\theta_4 + i\omega k_4Z_1cos\theta_4$,

$C_{2j}^O = -2p_{26}k_j^2sin\theta_jcos\theta_j + i\omega k_jZ_2sin\theta_j$, $C_{23}^O = -p_{26}k_4^2sin^2\theta_4 + p_{26}k_4^2cos^2\theta_4 - i\omega k_4Z_2cos\theta_4$, $C_{3j}^O = ir_jk_j \cos\theta_j + \omega Z_3r_j$,
$C_{33}^O = 0$, *j=1, 2.*

For incident P- Wave, T- wave

$F^* = F_{0J}$, $Y_1^O = p_{23}k_j^2cos^2\theta_O + p_{22}k_j^2sin^2\theta_O + p_{24}r_j + i\omega k_jZ_1cos\theta_O, Y_2^O = -2p_{26}k_j^2sin\theta_Ocos\theta_O - i\omega k_jZ_2sin\theta_O$,

$Y_3^O = ir_1 k_j \cos\theta_O - \omega Z_3 r_j$,   j=1,2 (P,T).

For incident SV-Wave:

$F^* = F_{04},\ Y_1^O = -(p_{23} - p_{22}) k_4^2 sin\theta_O cos\theta_O - i\omega k_4 Z_1 sin\theta_O, Y_2^O = p_{26} k_4^2 sin^2\theta_O - p_{26} k_4^2 cos^2\theta_O + i\omega k_4 Z_2 cos\theta_O, Y_3^O = 0.$

Appendix-VI

$C_{1j}^{OO} = -p_{23} k_j^2 cos^2\theta_j - p_{22} k_j^2 sin^2\theta_j - p_{25} s_j + i\omega k_j Z_1 cos\theta_j, C_{13}^{OO} = -(p_{23} - p_{22}) k_4^2 sin\theta_4 cos\theta_4 + i\omega k_4 Z_1 cos\theta_4,$

$C_{2j}^{OO} = -2p_{26} k_j^2 sin\theta_j cos\theta_j + i\omega k_j Z_2 sin\theta_j\, , C_{23}^{OO} = -p_{26} k_4^2 sin^2\theta_4 + p_{26} k_4^2 cos^2\theta_4 - i\omega k_4 Z_2 cos\theta_4\ ,$

$C_{3j}^{OO} = is_j k_j \cos\theta_j + \omega Z_4 s_j\ , D_{33}^{OO} = 0,$ (j=1, 2).

For incident P-Wave, P_o − Wave:

$F^* = F_{01}, F^* = F_{03},\ Y_1^{OO} = p_{23} k_j^2 cos^2\theta_O + p_{22} k_j^2 sin^2\theta_O + p_{25} s_j + i\omega k_j Z_1 cos\theta_O\ ,$

$Y_2^{OO} = -2p_{26} k_j^2 sin\theta_O cos\theta_O - i\omega k_j Z_2 sin\theta_O\, , Y_3^{OO} = is_j k_j \cos\theta_O - \omega Z_4 s_j$ $j = 1,2$(P, P_o).

For incident SV-Wave:

$F^* = F_{04},\ Y_1^{OO} = -(p_{23} - p_{22}) k_4^2 sin\theta_O cos\theta_O - iZ_1 \omega k_4 sin\theta_O, Y_2^{OO} = p_{26} k_4^2 sin^2\theta_O - p_{26} k_4^2 cos^2\theta_O + i\omega k_4 Z_2 cos\theta_O\ , Y_3^{00} = 0.$

Appendix-VII

$C_{1j}^{O1} = -p_{23} k_j^2 cos^2\theta_j - p_{22} k_j^2 sin^2\theta_j - p_{24} r_j - p_{25} s_j\ ,\ C_{14}^{O1} = -(p_{23} - p_{22}) k_4^2 sin\theta_4 cos\theta_4\ , C_{2j}^{O1} = -2p_{26} k_j^2 sin\theta_j cos\theta_j\ ,$

$C_{24}^{O1} = -p_{26} k_4^2 sin^2\theta_4 + p_{26} k_4^2 cos^2\theta_4\ , C_{3j}^{O1} = ir_j k_j \cos\theta_j\ , C_{34}^{O1} = 0\ , D_{4j}^{O1} = is_j k_j \cos\theta_j\ ,\quad C_{44}^{O1} = 0,$ (j=1, 2, 3).

For incident P-Wave, P_o- Wave, T-Wave:

$F^* = F_{0j}\ ,\ Y_1^{O1} = p_{23} k_j^2 cos^2\theta_O + p_{22} k_j^2 sin^2\theta_O + p_{24} r_j + p_{25} s_j\ , Y_2^{O1} = -2p_{26} k_j^2 sin\theta_O cos\theta_O\ , Y_3^{O1} = ir_j k_j \cos\theta_O\ ,$

$Y_4^{O1} = is_j k_j \cos\theta_O\ ,$ j=1,2,3(P, P_o,T).

For incident SV-Wave:

$F^* = F_{04},\ Y_1^{O1} = -(c_{23} - c_{22}) k_4^2 sin\theta_O cos\theta_O\ ,\ Y_2^{O1} = c_{26} k_4^2 sin^2\theta_O - c_{26} k_4^2 cos^2\theta_O\ , Y_3^{O1} = 0,\ Y_4^{O1} = 0.$

References

1. Lord, H. W. and Shulman, Y. (1967). A generalized dynamical theory of thermoelasticity. *Journal of the Mechanics and Physics of Solids*, 15(5), 299-309.
2. Green, A. E. and Lindsay, K. (1972). Thermoelasticity. *Journal of elasticity*, 2(1), 1-7.
3. Green, A. E., & Naghdi, P. (1991). A re-examination of the basic postulates of thermomechanics. *Proceedings of the Royal Society of London. Series A: Mathematical and Physical Sciences*, 432(1885), 171-194.

4. Green, A. E. and Naghdi, P. (1992). On undamped heat waves in an elastic solid. *Journal of Thermal stresses*, *15*(2), 253-264.
5. Green, A. E. and Naghdi, P. (1993). Thermoelasticity without energy dissipation. *Journal of elasticity*, *31*(3), 189-208.
6. Chandrasekharaiah, D. S. (1998) Hyperbolic thermoelasticity. *Applied Mechanics Reviews*, 51, 705–729
7. Nowacki, W. (1976) Dynamical problems of diffusion in elastic. *Journal of elasticity*, 8, 261–266,
8. Sherief, H. H., Hamza, F. A., and Saleh, H. A. (2004). The theory of generalized thermoelastic diffusion. *International journal of engineering science*, 42(5-6), 591-608.
9. Kumar, R., and Kansal, T. (2010). Dynamic problem of generalized thermoelastic diffusive medium. *Journal of mechanical science and technology*, *24*(1), 337-342.
10. Kumar, R., Ghangas, S., and Vashishth, A. K. (2022). Wave behavior at the interface of inviscid fluid and nl bio-thermoelastic diffusive media. *Biomaterials and Biomedical Engineering*, 6(1), 011.
11. Sharma, K. (2012). Reflection of plane waves in thermodiffusive elastic half-space with voids. *Multidiscipline Modeling in Materials and Structures*, 8(3), 269-296.
12. Sharma, S., Devi, S., Kumar, R., and Marin, M. (2025). Examining basic theorems and plane waves in the context of thermoelastic diffusion using a multi-phase-lag model with temperature dependence. *Mechanics of Advanced Materials and Structures*, 32(8), 1810-1827.
13. Chirilă, A. and Marin, M. (2021). Wave propagation in diffusive microstretch thermoelasticity. *Mathematics and Computers in Simulation*, 189, 99-113.
14. Eringen, A. C. and Edelen, D. (1972). On nonlocal elasticity. *International journal of engineering science*, *10*(3), 233-248.
15. Eringen, A. C. (1974). Theory of nonlocal thermoelasticity. *International Journal of Engineering Science*, *12*(12), 1063-1077.
16. Yu, Y. J., Tian, X. G., and Xiong, Q. L. (2016). Nonlocal thermoelasticity based on nonlocal heat conduction and nonlocal elasticity. *European Journal of Mechanics-A/Solids*, *60*, 238-253.
17. Saeed, T. and Abbas, I. (2022). Effects of the nonlocal thermoelastic model in a thermoelastic nanoscale material. *Mathematics*, *10*(2), 284.
18. Ezzat, M. A., El-Karamany, A. S., and Samaan, A. A. (2004). The dependence of the modulus of elasticity on reference temperature in generalized thermoelasticity with thermal relaxation. *Applied Mathematics and Computation*, *147*(1), 169-189.
19. Wang, Y. Z., Liu, D., Wang, Q., and Zhou, J. Z. (2016). Thermoelastic behavior of elastic media with temperature-dependent properties under transient thermal shock. *Journal of Thermal Stresses*, *39*(4), 460-473.
20. Zenkour, A. M. and Abouelregal, A. E. (2017). Laser pulse heating of a semi-infinite solid based on a two-temperature theory with temperature dependence. *Journal of Molecular and Engineering Materials*, *5*(03), 1750008.
21. Abouelregal, A. E. and Marin, M. (2020). The response of nanobeams with temperature-dependent properties using state-space method via modified couple stress theory. *Symmetry*, *12*(8), 1276.
22. Alharbi, A. M., Abd-Elaziz, E. M., and Othman, M. I. (2021). Effect of temperature-dependent and internal heat source on a micropolar thermoelastic medium with voids under 3PHL model. *ZAMM-Journal of Applied Mathematics and Mechanics/Zeitschrift für Angewandte Mathematik und Mechanik*, *101*(6), e202000185.
23. Sharma, S., Kumar, R., Taha, H. H., El-Bary, A. A., and Lotfy, K. (2025). Fundamental theorems and wave dynamics in rotating thermoelastic diffusion with multi-phase delays and temperature-dependent properties. *Rev. int. métodosnumér. cálc. diseñoing*, *41*(2), 34.
24. Said, S. M., Othman, M. I., and Eldemerdash, M. G. (2025). Effect of temperature-dependent properties and gravity on a nonlocal poro-thermoelastic medium with MDD via GL Model. *Journal of Vibration Engineering & Technologies*, *13*(1), 116.
25. Quintanilla, R. (2019). Moore–gibson–thompson thermoelasticity. *Mathematics and Mechanics of Solids*, *24*(12), 4020-4031.
26. Fernández, J. R., and Quintanilla, R. (2021). Moore-Gibson-Thompson theory for thermoelastic dielectrics. *Applied Mathematics and Mechanics*, *42*(2), 309-316.
27. Bazarra, N., Fernández, J. R., and Quintanilla, R. (2021). On the decay of the energy for radial solutions in Moore–Gibson–Thompson thermoelasticity. *Mathematics and Mechanics of Solids*, *26*(10), 1507-1514.
28. Abouelregal, A. E., Ahmed, I. E., Nasr, M. E., Khalil, K. M., Zakria, A., and Mohammed, F. A. (2020). Thermoelastic processes by a continuous heat source line in an infinite solid via Moore–Gibson–Thompson thermoelasticity. *Materials*, *13*(19), 4463.
29. Marin, M., Öchsner, A., and Bhatti, M. M. (2020). Some results in Moore-Gibson-Thompson thermoelasticity of dipolar bodies. *ZAMM-Journal of Applied Mathematics and Mechanics/Zeitschrift für Angewandte Mathematik und Mechanik*, *100*(12), e202000090.

30. Hobiny, A., and Abbas, I. (2025). Thermoelastic Responses of Living Tissues with and without Energy Dispassion Using the Eigenvalue Approach. *Mechanics of Solids*, *60*(1), 352-364.
31. Abouelregal, A. E., Ahmad, H., Nofal, T. A., and Abu-Zinadah, H. (2021). Moore–Gibson–Thompson thermoelasticity model with temperature-dependent properties for thermo-viscoelastic orthotropic solid cylinder of infinite length under a temperature pulse. *Physica Scripta*, *96*(10), 105201.
32. Kumar, R., Sharma, N., and Rani, V. (2026). A comprehensive examination of fundamental solution and Green's function in orthotropic photothermoelastic media including moisture. *Journal of Thermal Stresses*, *49*(4), 527-559.
33. Li, X. and Shao, H. (2024). Investigation of bio-thermo-mechanical responses based on nonlocal elasticity theory and fractional Pennes equation. *Applied Mathematical Modelling*, *125*, 390-401.
34. Tzou, D. Y. (1995) A unified field approach for heat conduction from micro to macroscales, *ASME Journal of Heat Transfer*, 117, 8–16
35. Guo, X., Chen, H., Zhu, X., Xia, A., Liao, Q., Huang, Y., and Zhu, X. (2021). Revealing the role of conductive materials on facilitating direct interspecies electron transfer in syntrophic methanogenesis: a thermodynamic analysis. *Energy*, *229*, 120747.
36. Rahman, F. M. M. and Banerjee, S. (2024). Peri-elastodynamic: Peridynamic simulation method for guided waves in materials. *Mechanical Systems and Signal Processing*, *219*, 111560.
37. Adel M., Raddadi M., El-Bary A. A., and Lotfy K. (2024). Mechanical-acoustic waves with two temperature nonlocal thermoelasticity theory subjected to decaying heat source. *Journal of Vibration Engineering & Technologies*, 12, 1767-1778.
38. Dhaliwal, R. and Singh, A. (1980) Dynamic coupled thermoelasticity. *Hindustan publishing corporation, New Delhi*
39. Tiersten, H. F. (1969). Elastic surface waves guided by thin films. *Journal of Applied Physics*, 40(2), 770-789.
40. Malischewsky, P.G. (1990) Surface Waves and Discontinuous, *Elsevier. Amsterdam*. 88:588.